



Article

# “Cape Fear”—A Hybrid Hillslope Plot for Monitoring Hydrological Processes

Flavia Tauro <sup>1</sup>, Andrea Petroselli <sup>2</sup> , Aldo Fiori <sup>3</sup>, Nunzio Romano <sup>4</sup> , Maria Cristina Rulli <sup>5</sup>, Maurizio Porfiri <sup>6</sup>, Mario Palladino <sup>4</sup> and Salvatore Grimaldi <sup>1,6,\*</sup>

<sup>1</sup> Department for Innovation in Biological Systems, Food and Forestry (DIBAF), University of Tuscia, 01100 Viterbo, Italy; flavia.tauro@unitus.it

<sup>2</sup> Department of Economics, Engineering, Society and Business Organization (DEIM), University of Tuscia, 01100 Viterbo, Italy; petro@unitus.it

<sup>3</sup> Dipartimento di Ingegneria, RomaTre University, 00146 Rome, Italy; aldo.fiori@uniroma3.it

<sup>4</sup> Department of Agricultural Sciences, AFB Division, University of Napoli Federico II, 80138 Napoli, Italy; nunzio.romano@unina.it (N.R.); mario.palladino@unina.it (M.P.)

<sup>5</sup> Dipartimento di Ingegneria Civile e Ambientale, Politecnico di Milano, 20133 Milan, Italy; mariacristina.rulli@polimi.it

<sup>6</sup> Department of Mechanical and Aerospace Engineering, New York University Tandon School of Engineering, Brooklyn, NY 11201, USA; mporfiri@nyu.edu

\* Correspondence: salvatore.grimaldi@unitus.it

Received: 16 May 2017; Accepted: 29 June 2017; Published: 4 July 2017

**Abstract:** Innovative experimental field designs and methods are instrumental for dissecting hydrological processes in hillslopes. However, experimental studies at the catchment scale are rarely affordable to most research groups, and laboratory flumes are oversimplified to reproduce natural phenomena. In this work, we present the innovative “hybrid” experimental plot of Cape Fear, which features controllable water fluxes and boundary conditions, but it is directly exposed to external atmospheric agents. We demonstrate the suitability of Cape Fear to study hydrological phenomena through a feasibility test, whereby the response of the plot to a natural storm is in line with the well-known hydrological response of natural hillslopes. Future studies will address the influence of the plot geometry parameters on rill formation.

**Keywords:** cape fear; hillslope processes; experimental plot; runoff onset; soil moisture; rill formation; tracers; fluorescent particles

## 1. Introduction

Hydrological processes occurring at the hillslope scale highly influence the response of natural catchments [1]. Over the years, considerable efforts have been devoted to the identification of the mechanisms through which hillslopes store and release water [2,3]. In this respect, experimental studies have been fundamental to improving our current comprehension of major phenomena underlying runoff formation. In [4,5], the quick rise in runoff flow during rainfall was related to the concept of variable source area. Such mechanism was later verified and the concept of partial area contribution was formulated by [6,7]. In [8,9], data from experimental observations were utilized to relate soil moisture and matric potential flow field to topography.

Despite the abundance of hillslope studies, hillslope processes are still far from being a closed topic. In [10], innovative experimental field designs and methods to improve hillslope modelling were clearly advocated. Several decades later, the need for field observations is still motivated by the complexity of hillslope phenomena that are influenced by diverse environments and can significantly vary in different parts of the same catchment.

Large scale natural slopes are ideal toward an improved understanding of hydrological processes [11,12]. For instance, in [13], the hydrological response of two densely instrumented zero-order catchments in the Oregon Coast Range was studied. The response of such unchannelled valleys to natural and artificial rainfall has been thoroughly investigated with traditional instrumentation and tracer techniques [14,15], and has shed light on the timing and contribution of new/old water to runoff. Extensive field experiments have also been conducted in the 41 ha Panola Mountain Research catchment. Field data captured therein have enabled investigations on the role of bedrock topography on subsurface storm flow [16], leading to the formulation of the fill and spill hypothesis [17–19]. The Maimai research catchments in New Zealand has been intensively studied since the late 1970s and has provided precious insights on the role of riparian zones within the catchment [20]. Furthermore, the catchment-scale Hydrological Open Air Laboratory (HOAL) in Lower Austria is a 66 ha laboratory [21], which is an extremely rich testbed for the comprehension of water flow and transport processes. Finally, the 6 ha artificial catchment “Chicken Creek” serves as a laboratory for interdisciplinary ecological research [22]. While field campaigns at the catchment scale are necessary in hydrology, the complexity of site geometry and uncertainties in boundary conditions and water fluxes mandate long-term and frequent observations, which are rarely affordable to research teams.

Alternative to catchment-scale studies, the response of hillslopes has also been investigated by isolating experimental plots in natural watersheds [23]. For instance, in [24], runoff generation is attributed to soil surface crusting in  $0.5 \times 0.5 \text{ m}^2$  plots located in various zones of a real hillslope. In [25], plastic and metal sheeting is utilized to study the response of a  $35 \times 18 \text{ m}^2$  slope in a natural field, and a methodology to measure lateral saturated hydraulic conductivity is illustrated. Similarly, in [26], trenches are excavated at numerous  $4 \times 15 \text{ m}^2$  natural hillslope sites to monitor runoff formation during intense artificial precipitation. Therein, interactions between infiltration rate, change in soil water storage, and drainage of the soil water were shown to control runoff processes. The effect of vegetation on water fluxes and erosion is investigated in [27]; overland flow times on artificial slopes are studied in [28]; and the effect of vegetation and ground cover on erosion is analyzed through three small scale plots in [29]. Simple facilities to study overland flow, infiltration, and soil moisture are also presented in [30,31]. These studies offer the advantage of experimenting with natural soil structure. However, similar to catchment-scale studies, controlling water fluxes may be challenging.

Constructed plots offer great potential for hillslope hydrology. In fact, they enable enhanced controllability of input fluxes, repeatability of investigations, and a priori determined boundary conditions. An outstanding example is the Biosphere 2 Hillslope Experiment, Oracle, Arizona, where a system of three  $18 \times 33 \text{ m}^2$  hillslopes has been assembled to study the evolution of soil, water, and biota [32,33]. The design of this unique facility involves several research groups and is expected to open novel perspectives for a unifying hydrological theory at the catchment scale.

Most frequently, constructed plots and flumes have been utilized to test simplified hypotheses. Such flume-scale studies are conducted in artificially assembled outdoor or indoor facilities of a few squared meters. In [34], two-dimensional flow of soil moisture under rainfall infiltration has been studied in a flume with homogeneous soil. In [35], the influence of slope length on runoff has been investigated in a flume filled with uniform soil. A similar study on the effects of rill erosion on runoff and sediment yielding has been more recently conducted by [36] in an experimental flume with adjustable slope. In [37], a 1:100 laboratory flume enabled investigations on the coupling between hillslope and river channel during rainfall through several experimental configurations and replicates. Finally, in [38], the interplay among runoff, soil loss, and rill development was dissected in plots of adjustable slope, homogeneous soil, and under artificial rainfall intensities. Such flume/plot-scale facilities are generally adopted to test hydrological models, and present homogeneous soil, basic monitoring equipment, or mostly artificial rainfall conditions.

Cape Fear is a “hybrid” outdoor hillslope plot for testing fundamental hypotheses on runoff generation processes. The novelty of the plot consists of combining features from both laboratory facilities and catchment-scale experimental hillslopes. Similar to laboratory boxes, Cape Fear is a

confined soil-filled wood-sided plot, whose water fluxes can be controlled and where infiltration to deeper soil layers is hampered. On the other hand, similar to natural instrumented slopes, the plot is subject to external agents, such as rainfall and temperature.

The “intermediate” features of Cape Fear offer several advantages for hydrological observations. First, simplified and controllable geometry and morphology allow for easily identifying the magnitude and characteristics of hydrological processes taking place in the plot, thus facilitating accurate water balance closure estimations. Second, the facility enables controllability of water fluxes through real time observations with a low cost sensing infrastructure. Sensing equipment can be easily rearranged (for instance, the soil and slope of the plot can be modified, along with the instrument location) according to specific experimental requirements. Finally, even if simplified geometry and limited natural soil structure prevent the establishment of hydrological processes found in natural ecosystems, the setup is directly exposed to external events, thus allowing for investigating the response of the plot to natural atmospheric conditions. For instance, we expect that the plot exposure to natural rainfall and temperature conditions would provide insightful feedback for the comprehension of runoff formation.

In this work, we present the innovative experimental plot of Cape Fear by reporting detailed and specific technical information on sensing instrumentation and plot geometry. In addition, we demonstrate the suitability of Cape Fear to study hydrological phenomena through a feasibility test, whereby we reconstruct the response of the plot to the natural precipitation event occurred on 30 January 2014, through sensing instrumentation permanently installed at Cape Fear and with the high-visibility surface tracer previously adopted in [39–41].

## 2. Materials and Methods

### 2.1. Experimental Site

#### 2.1.1. Plot Description

Cape Fear is realized in a terrain parcel in the Azienda Agraria at the University of Tuscia, Viterbo, Italy. The plot extends on an area of  $7 \times 7 \text{ m}^2$ , is constructed out of  $40 \text{ m}^3$  of soil, and has an average slope of 17% (see Figure 1a). The plot comprises  $30 \text{ m}^3$  of natural soil, whereby additional  $10 \text{ m}^3$  constitute its foundation. Plot assembly occurred from May to November 2014 and its main phases were: (i) foundation laying (during foundation, soil was compacted and then left to settle for a few months); (ii) assembly and installation of the wood containment structure on three sides; (iii) installation of the waterproof layer; and (iv) installation of soil. During the last phase, soil was laid in layers and then compacted. The waterproof layer prevented infiltration to the underlying soil, thus acting as an impermeable bedrock and facilitating water budget estimations. The lower end of the slope was opened and allowed to freely drain, thus promoting saturated overland flow as driving mechanism for runoff formation. The rather invasive plot assembly allows for a priori controlled geometry and boundary conditions. A system of four rainfall simulators, based on the instrument adopted in [42] and initially developed in [43], is installed in the hillslope to uniformly irrigate the plot. Rainfall is provisioned and regulated through a water feeding system, including a tank, a hydraulic pump, a flow meter, and a buried piping (see Figure 1b).

The experimental site features a real-time monitoring system, which affords the acquisition of data on input artificial and natural rainfall, output water discharged from the plot, turbidity, soil moisture conditions, and qualitative information on the wetting front propagation. Acquired values are recorded and stored by a CR10X Campbell Scientific datalogger (Logan, UT, USA). The logger records data every second from all the installed instruments. Since the used measuring interval of instruments connected to the datalogger was set to five minutes, data captured every second are then averaged over time intervals of five minutes and stored for maximum periods of ten days.

As displayed in Figure 1c, the site includes a working region where undisturbed conditions are maintained. The region is a  $4 \times 4 \text{ m}^2$  square with the rainfall simulators located at its vertices. Around

the working region (where access is forbidden to preserve natural soil surface structure), 1.5 m-wide sections are left from the external side of the hillslope to mitigate border effects.



**Figure 1.** (a) view of the hillslope experimental plot during a sensor calibration experiment; (b) rainfall feeding system; and (c) view of the working region.

### 2.1.2. Soil Physical and Hydrological Characterization

Cores were obtained from the uppermost 20 cm of the plot by driving a steel cylinder vertically into the soil. A hand-operated device was used while excavating by hand the soil around the cylinder to limit disturbances during sampling. In Figure 2, the locations of the soil core samples are indicated in a plane sketch view of the plot. The soil cores were collected using steel cylinders of about 0.07–0.08 m in diameter. In experiments on the suction table (soil cores collected at locations from P02 to P05), steel cylinders are 0.07 m in height. Furthermore, an evaporation experiment was conducted on a 0.15 m core collected at location P01. Before performing hydraulic tests, the top of each undisturbed soil core (a thickness of approximately 0.03–0.04 m) was removed and stored for particle-size analyses, organic content measurements, and for measuring soil water retention data in the dry range through pressure plate apparatus.

The particle-size distribution was determined using standard laboratory techniques based on a set of sieves and the soil hydrometer [44]. The organic carbon content was determined with the



dichromate method [45]. Saturated water content,  $\theta_{\text{sat}}$ , was measured by the gravimetric method [46], whereas the saturated hydraulic conductivity,  $K_{\text{sat}}$ , was measured by the falling-head method [47].

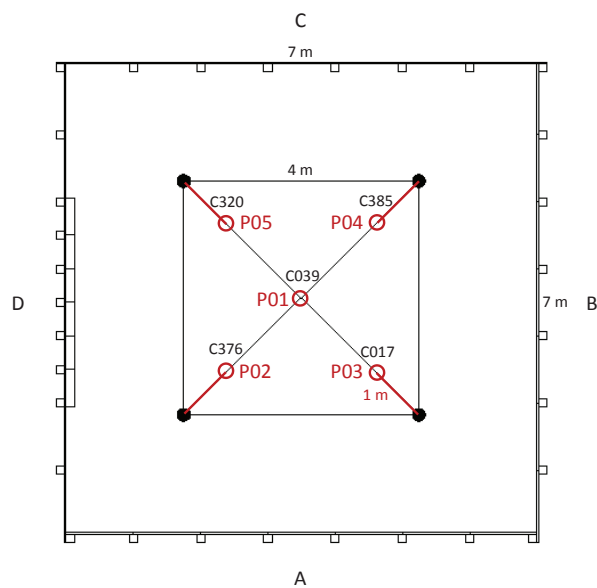


**Figure 2.** Plane sketch of the experimental plot: numbers indicate the location of soil samples, and codes refer to samples' naming convention. (A–D) are utilized to name the plot sides.

Table 1 reports the physicochemical and hydraulic properties of the collected soil samples. The small subset of soil cores collected during the first sampling campaign did not allow to obtain suitable information about the probability distributions of the soil parameters and their associated uncertainties. Therefore, reported values of conventional coefficient of variation (CV%) only provide the reader with a rough idea on the dispersion among available data.

As often confirmed in the literature, at the small space scale of the plot, the variability of the soil physical properties is relatively small. Specifically, CV% of oven-dry bulk density,  $\rho_b$ , is equal to 3.9%. Furthermore, the average of the coefficients of variation computed for soil texture components (% sand, % silt, and % clay contents) is approximately 7.5%. Soil size limits (sand: 2–0.05 mm; silt: 0.05–0.002 m; and clay: <0.002 mm) from the United States Department of Agriculture (USDA) textural classification system were adopted. Conversely, the CV% of organic C content is greater than the other soil properties and equal to 17.5%. Therefore, small variability in microporosity generated by primary particles (sand, silt, and clay), which characterize the “textural” behavior of the soil, should be expected. On the other hand, large variability in the macroporosity should be found due to the larger statistical dispersion of the binding agent (organic C content), which favors the formation of aggregates, or probably due to biological activity. This feature can be the major reason for the observed significant variability in  $K_{\text{sat}}$  (CV% equal to 163.3%). It is worth noting that such CV% value is typical for  $K_{\text{sat}}$ , even at the small space scale of the hillslope plot (see [48] among many others). The large variability in  $K_{\text{sat}}$  values is also attributable to the relatively small  $\rho_b$  measurements, which make the uppermost soil more prone to local compaction.

The four undisturbed soil cores (0.07 m in length and 0.072 m in diameter) excavated at locations P02 to P05 were collected from a soil depth of 0.05–0.12 m. After estimating  $\theta_{\text{sat}}$  and  $K_{\text{sat}}$  as outlined above, the cores were reduced in height to approximately 0.04 m. Then, they were placed on a suction table for directly measuring soil water retention points [49]. Soil water contents at greater suction head (lh) values, ranging from 75 kPa to 1200 kPa, were determined using a series of pressure plate extractors [50].

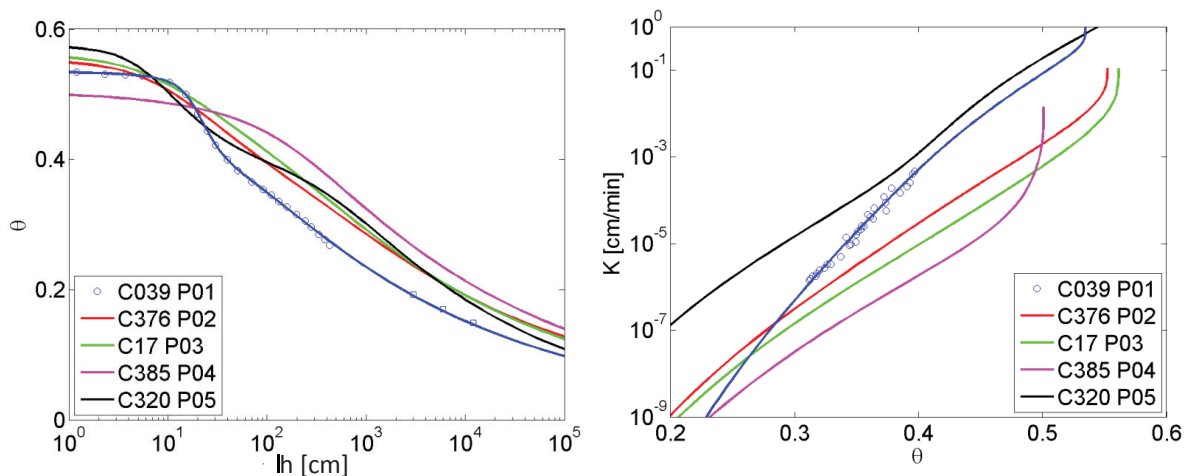
The soil water retention and hydraulic conductivity functions of the undisturbed soil core collected at location P01 were determined simultaneously in the laboratory using the evaporation experiment developed by [51].

Figure 3 shows the soil water retention,  $\theta(h)$ , and hydraulic conductivity,  $K(\theta)$ , functions (WRFs and HCFs, respectively), as determined by the two laboratory methods presented above. WRFs for the undisturbed cores tested in the suction table present a similar behavior when approaching drier soil conditions. This is due to the relatively small variations in the soil textural properties (see Table 1). As discussed for Table 1, larger differences among the WRFs occurred close to full saturation mainly due to the local and unpredictably different degrees of compaction and aggregation of the primary soil particles. Interestingly, the WRF of the soil core tested through the evaporation experiment showed a certain bimodal behavior, whose description through a bimodal relation leads to a much better prediction of  $K$  (as discussed in [52]), see the right panel of Figure 3.

In Figure 3, points obtained by processing measured data with a modified Wind's method match very well analytical findings, obtained through the evaporation inverse method developed by [53]. Importantly, HCFs of the soil cores collected at positions from P02 to P05 were simply predicted from WRFs parameters and from measured  $K_{\text{sat}}$  values. Differently, the HCF of the soil core collected at P01 was obtained simultaneously with the WRF from the measured variable during the evaporation experiments. The differences between the soil hydraulic properties of the cores at P02–P05 and those of the core at P01 can also be partially due to the different sizes of the cores (the core subjected to the evaporation experiment has a volume of about  $500 \text{ cm}^3$ , whereas the cores draining on the suction table have a volume of about  $250 \text{ cm}^3$ ). Furthermore, differences in HCFs of cores at P02–P05 are emphasized by variabilities in the measured values of  $K_{\text{sat}}$ , which is very sensitive to local compaction conditions.

**Table 1.** Hydraulic properties of the soil samples.

	C039 P01	C376 P02	C017 P03	C385 P04	C320 P05
$\rho_b$ ( $\text{g} \cdot \text{cm}^{-3}$ )	0.979	1.025	1.090	1.025	1.048
Organic C (%)	0.448	0.721	0.604	0.526	0.584
Sand content (%)	45.87	42.40	46.52	43.70	41.63
Silt content (%)	33.38	34.52	34.00	38.94	37.19
Clay content (%)	20.75	23.28	19.48	17.36	21.18
$\theta_{\text{sat}}$ ( $\text{cm}^3 \cdot \text{cm}^{-3}$ )	0.534	0.552	0.561	0.501	0.574
$K_{\text{sat}}$ ( $\text{cm} \cdot \text{min}^{-1}$ )	1.386	0.129	0.171	0.0363	5.737



**Figure 3.** Soil hydraulic properties of the soil cores collected in the study site: soil water retention functions (left); hydraulic conductivity functions (right). Circles and squares indicate measured data points obtained through the evaporation method and the pressure plate apparatus, respectively. Experimental data points for soil cores collected at P02–P05 are not displayed for clarity.

## 2.2. Observed Variables

### 2.2.1. Output Discharge

Water exiting the experimental plot is collected in a v-shaped aluminum channel extending along the downslope side of the plot (see Figure 4a). The channel discharges water and solids in an aluminum tank, where a water level sensor surveys output discharge rate. Such a tank is composed of three connected partitions (see Figure 4b). Water enters the first section of the tank, where coarser solid material is collected, up to the height of the separating screen. In the second section of the tank, water and finer sediments overflow from the first one. Water and suspended sediments enter the third partition of the tank through a rectangular aperture located at the bottom of the screen that separates the second and third partitions. Water flows out of the tank through a v-notch weir section and is drained into a low-lying agricultural ditch. A Structural Testing System (S.T.S.) strain gauge (S.T.S. global sensor excellence) detects the water level in the last partition of the aluminum tank.

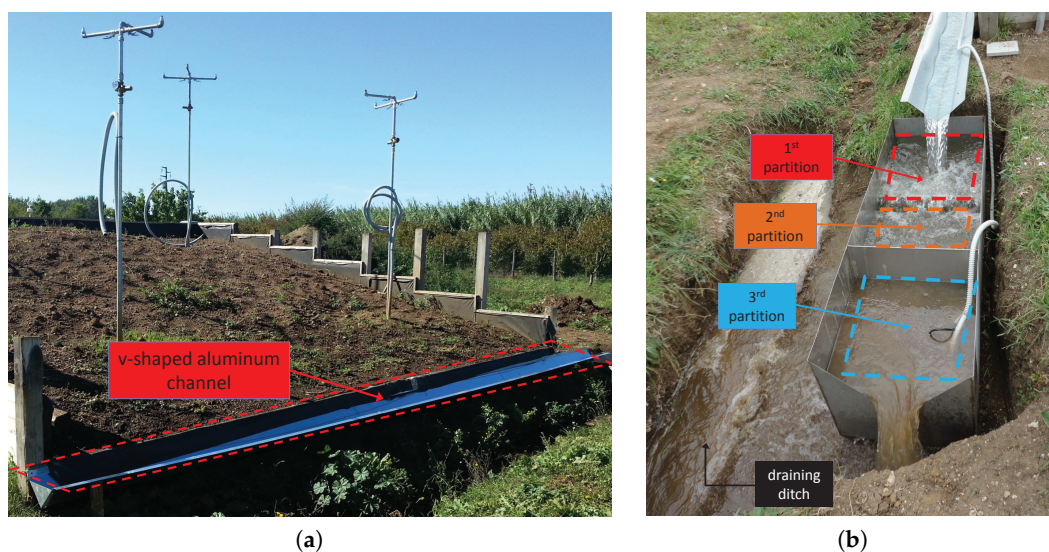


**Figure 4.** (a) V-shaped aluminum channel extending along the downslope side of the experimental plot and (b) collection tank comprising three partitions for sediment separation. The last partition of the tank features a v-notch weir section, a turbidity sensor probe, and a water level sensor to measure output discharge rates.

In Figure 5, the rating curve for the output discharge from the v-notch weir is presented. This relation was obtained by performing experiments where known discharges were fed into the aluminum tank and water levels were measured with the S.T.S. strain gauge. Experimental data in Figure 5 are fitted to obtain the rating curve, where  $Q$  and  $h$  are the output discharge and water height above the v-notch weir, respectively. Specifically, red dots are experimental measurements; the blue dashed line is a fitted power law; the green dotted line is a fitted polynomial law; the magenta solid line is the rating curve for sharp-crested weirs with triangular control section ( $\alpha$  is the angle between the sides of the notch) [54] and effective discharge coefficient ( $C_d$ ) function of the water head; and the dash-dotted black line is the rating curve for sharp-crested weirs with triangular control section with effective discharge coefficient equal to 0.6. Relation  $Q_1$  accurately fits experimental data ( $R^2 = 0.98$ ), and it is therefore used for discharge data processing.

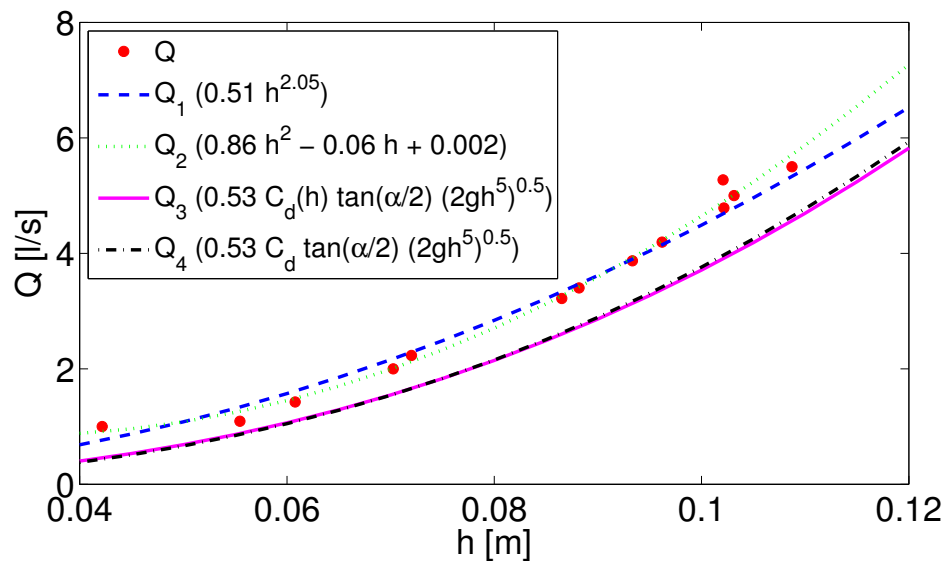


**Figure 5.** Relations between output discharge,  $Q$ , and water level,  $h$ , for the v-notch weir section of the collection tank.

### 2.2.2. Turbidity

In addition to the water level sensor, the collection tank hosts a stainless steel OBS-3+ turbidity sensor probe (2% accuracy). The probe allows for real-time measurements of the suspended solid material gathered in the final partition of the collection tank. Preliminary calibration experiments were performed to establish the relation between the suspended solid content (SSD) and the nephelometric turbidity units (NTU) measured by the probe. Specifically, soil specimens were gradually added to a tank filled with 100 L of water. The same soil used for the plot was used for calibration. Each soil sample was deployed at intervals of approximately 10 min and a total volume of 4.41 kg was loaded in the tank. Manual stirring was used to prevent sedimentation and homogenization of the sediments. In Figure 6, we report the linear relation between turbidity ( $T$ ) in NTU units and the suspended solid content in the tank. The linear relation accurately fits experimental data ( $R^2 = 0.95$ ).

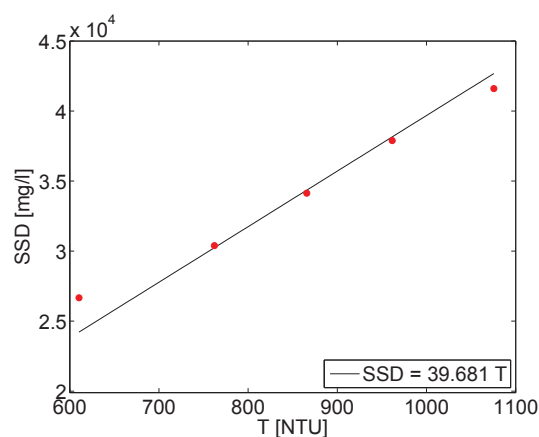


**Figure 6.** Suspended solid concentration (SSD) in mg/L against turbidity ( $T$ ) in nephelometric turbidity units (NTU) as recorded by the turbidity sensor.

### 2.2.3. Soil Moisture

Soil moisture in the plot is monitored through four Campbell Scientific CS615 water content reflectometers. Such instruments can be oriented both vertically and horizontally to sense the water



content in the soil. During experimental tests, the four probes were inserted in the working area of the hillslope plot as illustrated in Figure 7 to monitor soil moisture. Specifically, probes were installed after the soil was packed by digging soil pits. Measurement rods were thrust into the soil at 10 and 50 cm depths horizontally underneath the working region of the plot, thus causing minimal disturbance.

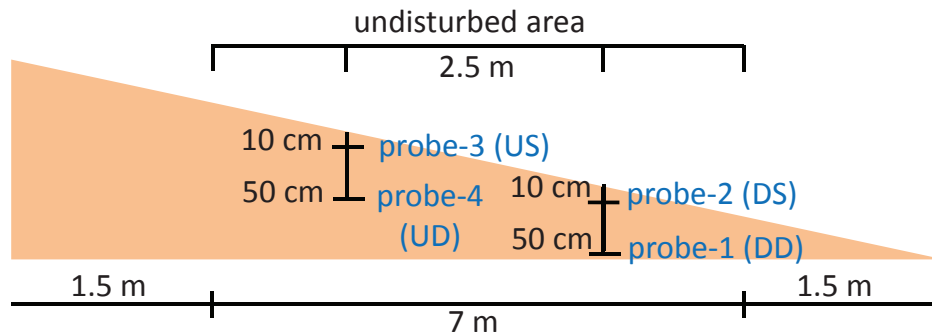


**Figure 7.** Location of the soil moisture probes in the experimental plot. The sensors are aligned along the downslope direction in the center of the plot. According to their location, probes are named using acronyms. The acronym UD stands for upslope-deep, US for upslope-shallow, DS for downslope-shallow and DD for downslope-deep.

To estimate the water content sensed by the probes at saturation, in situ experimental tests were conducted. Specifically, water was fed from the hillslope surface at the location of the probes for up to 24 h to facilitate moisture migration. Saturation was achieved after a 24 h-test for probes 2, 3 and 4. The upslope-deep probe gained a maximum value of 0.422; the upslope-shallow probe sensed a maximum of 0.462; and the downslope-shallow probe attained a maximum of 0.364. The downslope-deep probe achieved a maximum of 0.503 after a 21 h-test.

#### 2.2.4. Wetting Front

Subsurface wetting front propagation is visually monitored through a row of three glass panels (each with dimensions of 80 cm in width, 24 mm in thickness, and with increasing heights of 70, 90 and 110 cm) installed on the left wall (facing upslope) of the plot, see Figure 8. Estimations are conducted by periodically capturing pictures of the infiltration profile, which is easily distinguishable due to the darker color of wet soil. Pictures are acquired with a GoPro Hero 2 (GoPro Inc., San Mateo, CA, USA) set to high resolution and low acquisition frequencies. The camera is installed at approximately 1 m from the central glass panel to capture pictures every 15 min. Direct reflections from sunlight and the detrimental effect of raindrops were accounted for by installing a platform roof above the glass panels. Figure 8 displays a picture of the infiltration profile acquired during a validation experiment.



**Figure 8.** View of the wetting front observed through the glass panels during a validation experiment.

### 2.2.5. Rainfall Gauge

Rainfall is monitored through the available rain gauge system located in the same terrain parcel at 20 m from the hillslope plot [55]. The rain gauging apparatus consists of a system of four SBS-500 Campbell Scientific standard tipping bucket collectors (collector area of 500 cm<sup>2</sup> and tip sensitivity of 0.2 mm) connected to a datalogger. Consistent with the sensing apparatus on the hillslope plot, rainfall measurements are recorded every 5 min from each collector. The collectors are evenly spaced at the corners of a 10 × 10 m<sup>2</sup> square and rainfall values averaged over the four recordings are used to estimate input precipitation.

### 2.2.6. Artificial Rainfall System

The artificial rainfall system is based on four pressurized nozzle rainfall simulators equipped with pressure probes [30,56]. Simulators were designed and developed based on the prototype by [43] and are consistent with the simulator presented in [42]. Their structure comprises a telescopic aluminum tripod connected to a steel plate. Three hoses are riveted to the plate and water is sprayed through a system of three nozzles. An HH7-M 3/4 in nozzle is mounted on the central hose whereas two smaller HH22-M 3/8 in nozzles are placed onto the lateral hoses. Three cut-off valves allow for selectively activating the nozzles and controlling rainfall intensity. Rainfall intensities can be varied from a minimum of 40 mm · h<sup>-1</sup> by using the two smaller nozzles to 140 mm · h<sup>-1</sup> by operating the three nozzles simultaneously.

Calibration experiments for assessing the uniformity and intensity (*I*) of one rainfall simulator were conducted in an outdoor space at University of Tuscia where wind effects are minimal. Micro rain gauges were distributed on the nodes of a 7 × 7 m<sup>2</sup> square grid at the reciprocal distance of 1 m and with the simulator positioned at the center of the square. A similar characterization of a rainfall simulator was conducted by [57]. The diameter of the rain gauges was equal to 68 mm. The simulator was tested for the following configurations of the nozzles: the two HH22-M 3/8 in nozzles were activated (C1); one HH22-M 3/8 in and the HH7-M 3/4 in nozzle were opened (C2); and each nozzle was opened and sprayed (C3). Experiments were conducted by varying the pressure of the simulator from 0.4 to 1.8 bar. During each experiment, the simulator was activated at a constant pressure (*H*) for a duration of 15–45 min. At the end of the experiment, rain gauges were weighted and rain intensity values were obtained for each node of the square grid. Four repetitions were conducted for each nozzle configuration. Rainfall intensities computed over uniform space grids of 3 × 3 m<sup>2</sup> and 5 × 5 m<sup>2</sup> are displayed in Figure 9.

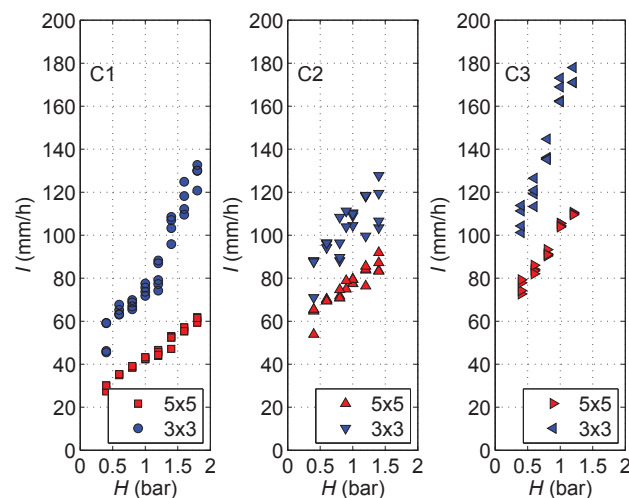


**Figure 9.** Rainfall intensity (*I*) versus pressure (*H*) during rainfall simulator calibration experiment for configuration C1 (left), C2 (center), and C3 (right).

A characterization of the spatial rainfall variability of the simulator was assessed by computing the coefficient of uniformity (CU). As introduced in [58], CU is defined as

$$CU = 100 \left( 1 - \left( \frac{\sum_{i=1}^{i=n} |X_i - \bar{X}|}{\bar{X}} \right) \right), \quad (1)$$

where  $X_i$  is the rainfall intensity obtained from a single micro rain gauge,  $\bar{X}$  is the mean rainfall intensity, and  $n$  is the number of available rainfall data. Mean percentage values for CU are reported in Table 2 for each experimental configuration.

**Table 2.** Coefficient of uniformity (CU) for the three rainfall simulator configurations. Entries are average CU values obtained by varying the water pressure from 0.4 to 1.8 bar.

Configuration	C1	C2	C3
CU (%) $3 \times 3 \text{ m}^2$	75	82	82
CU (%) $5 \times 5 \text{ m}^2$	32	66	61

As expected, good uniformity was obtained for each configuration in case of the smaller area. Nonetheless, acceptable values were also found for the  $5 \times 5 \text{ m}^2$  area for configurations C2 and C3. Lower CU values for configuration C1 are related to the fact that the two HH22-M 3/8 in nozzles unevenly distribute rain on the surface of interest. This effect is compensated for when the HH7-M 3/4 in nozzle is active.

Drop size distribution (DSD) and velocity were characterized through calibration experiments with the OTT Parsivel optical disdrometer (OTT Hydromet, Loveland, CO, USA). Specifically, the rainfall simulator nozzles were placed at approximately 1.5 m above the optical disdrometer and were activated for approximately 15 min. Two repetitions were conducted for each experimental configuration (C1, C2, and C3). During the experiment, pressure was varied in the range 0.4–0.6 bar. After each calibration experiment, the number of hydrometeors for 32 classes of diameters and velocities was obtained. Average values obtained from the two repetitions are plotted in Figure 10. Here, experimental values are compared to commonly used empirical relations by [59–61]. The majority of the drop diameters ( $D$ ) concentrates around 1 mm. This value is in good agreement with real drop size distribution data as illustrated in [30,62].

On the other hand, velocity of the rainfall simulator drops ( $V$ ) tends to be lower than naturally observed data for cases C2 and C3. We may attribute this evidence to the fact that the simulator nozzles are placed at only 1.5 m above the disdrometer. Higher velocities at small diameters were instead obtained for case C1. These results may be due to the uneven rain distribution of configuration C1, and, therefore, suggest that the use of the two HH22-M 3/8 in nozzles is not ideal for simulating natural precipitations. Colorbar in Figure 10 indicates the percentage number of drops for each class of diameter and velocity. In Figure 10, the majority of the hydrometeors' diameters and velocities lay in the proximity of empirical values from [59–61]. This confirms that simulated rainfall is representative for natural precipitations when configuration C2 and C3 are adopted and, therefore, alleges the feasibility of replicating natural rainfall in the  $4 \times 4 \text{ m}^2$  working region at Cape Fear using the system of four artificial simulators.

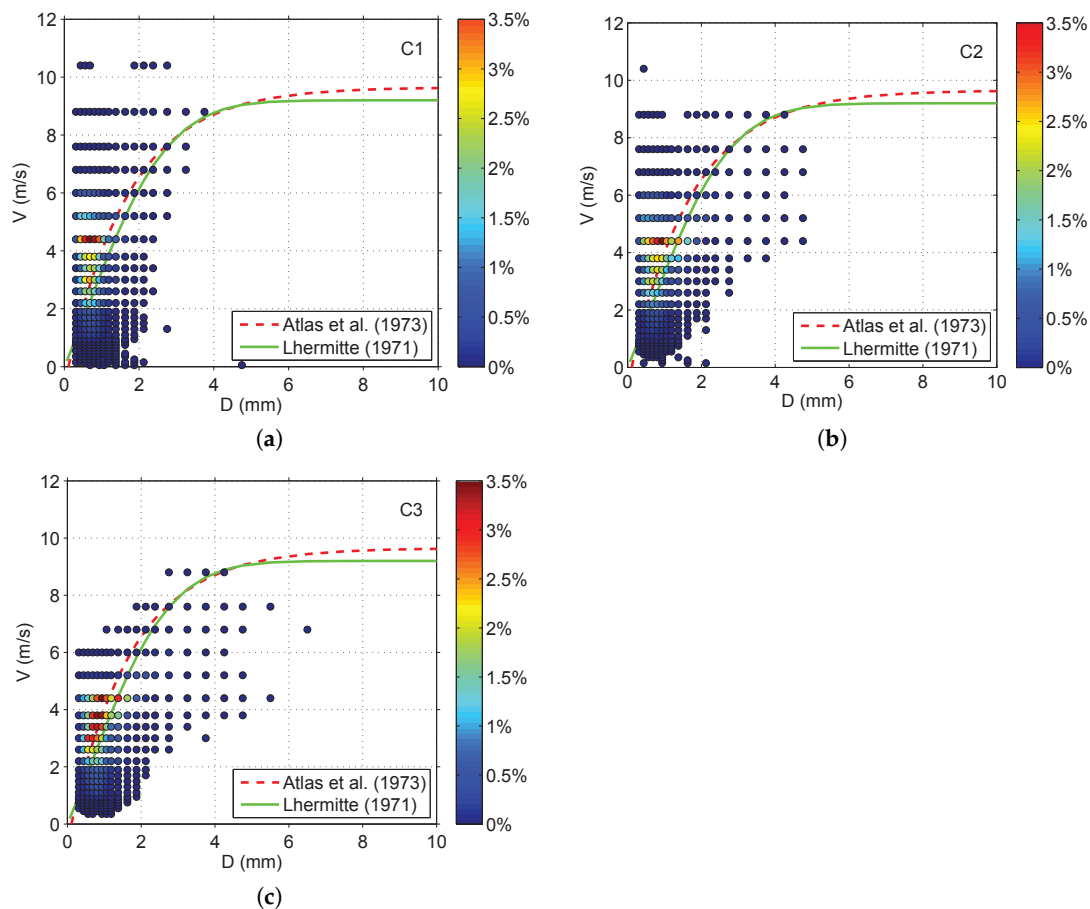


**Figure 10.** Drop diameter ( $D$ ) vs velocity ( $V$ ) for the (a) C1; (b) C2; and (c) C3 configurations. Colorbar indicates the percentage of hydrometeors for combinations of velocity and diameter. The red dashed curve is obtained through the empirical relation by [59]  $V = 9.65 - 10.3e^{-0.6D}$ , whereas the green solid curve corresponds to the relation developed in [60],  $V = 9.2[(1 - e^{-(0.11D^2+0.33D)})]$ .

### 2.3. Feasibility Experiment

#### 2.3.1. Rainfall Event

The feasibility of studying runoff generation processes at Cape Fear was assessed by conducting an experiment driven by a natural rainfall event. Specifically, we observed and studied the plot hydrological regime for a time window of 30 h, from 10:00 on 29 January 2014 to 16:00 on 30 January 2014. During such a time, rainfall first occurred in the night between 29 and 30 January, and then in the afternoon on 30 January. Prior to the experiment, the hillslope was left uncovered for two weeks to allow stable moisture and infiltration conditions to be established in the plot. During the experiment, input rainfall, output discharge, suspended sediment concentration, and soil moisture were measured every five minutes. Furthermore, we utilized a fluorescent particle tracing system to investigate the onset of surface runoff.

#### 2.3.2. Fluorescent Particle Sensing System

The onset of surface runoff on the plot was studied using buoyant fluorescent particles as surface tracers. In particular,  $0.98 \text{ g/cm}^3$  polyethylene beads purchased from Cospheric LLC (Santa Barbara, CA, USA) were used to trace surface runoff. When exposed to UV light (365 nm wavelength), the particles emit green light radiation (561 nm wavelength). We deployed a few grams of fluorescent particles in the area illustrated in Figure 11, that is, in between the working region and the downslope



1.5 m-wide border. In this region, moisture is considerable as indicated by the rather dark soil coloring, and saturation is more likely to occur in short time periods. The beads were deployed on the hillslope at the start of rainfall, that is, at about 11:18 on 30 January, over a rectangular area extending for  $50 \times 30 \text{ cm}^2$ . The tracer particles were transported on the plot surface and then on the v-shaped aluminum channel located along the downslope side of the hillslope. They were further gathered on the surface of the second partition of the collection tank where the detection unit was placed, see Figure 12. The unit consists of a case with an array of fourteen UV 8 W lamps in parallel and series connections. The case is waterproof and lamps are protected from water through a transparent plastic screen. A GoPro Hero 3 was used to monitor particle arrival at the collection tank. The camera was held in a waterproof case and was angled to capture the entire surface of the second partition of the tank.

As demonstrated in [42], groups of particles as small as  $75 \mu\text{m}$  can be detected in case of rill flow on semi-natural hillslope plots. At the onset of the experiment, the soil surface in the working region did not display rill-like structures visible with a naked eye. Therefore, we investigated the initiation of runoff by selecting a mixture of particles of diverse diameters. Specifically, few grams of beads of diameters varying in the range from  $75$  to  $1180 \mu\text{m}$ , were mixed with larger quantities of  $710$ – $850 \mu\text{m}$  spheres. The particle detection camera was set to 12 MP image resolution and to 0.1 Hz frame acquisition rate. Opaque panels were kept above the lamp case to minimize the effect of rain and direct light.

Particle arrival in time was surveyed by analyzing the image pixel coverage pertaining to the fluorescent beads. Such coverage was expected to increase as more particles were transported in the collection tank during the experiment. More precisely, we converted captured RGB (red-green-blue) frames to gray-scale and performed a morphological segmentation analysis [63] to isolate the beads from the rest of the objects depicted in the images. To this end, we processed the frames with a filtering procedure that detects image edges. We further eroded images with structuring elements of the shape and size of the fluorescent particles and reconstructed frames by connecting the only background pixels. We subtracted the reconstructed images from the original frames to isolate the particles in the field of view. This procedure was performed on the entire sequence of approximately 700 frames recorded during the experiment. For each frame, we quantified the amount of pixels pertaining to the particles and normalized it with respect to the total pixel area of the frames to develop a breakthrough curve for the tracer.

In Figure 13, we report two snapshots recorded from the particle detection unit at the beginning and close to the end of the last observed rainfall peak on 30 January. Images depict the unprocessed original frames and the same images after the segmentation procedure, where the only particles are depicted against an artificial homogeneous background. Fluorescent spheres tended to align at the borders of the tank and along water surface ripples. While the methodology shows good accuracy in detecting the particles against light reflections and different floating objects, edges between the water and the tank were not completely subtracted from the background image. However, the percentage of image coverage pertaining to the tank edges was constant during the experiment and, thus, did not affect particle identification. Despite the small size of the particles, they were clearly detectable and quantity considerably increased during the experiment.

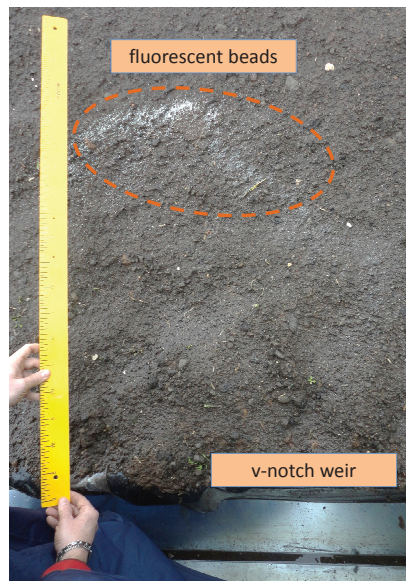


**Figure 11.** View of the fluorescent beads, white powder in the picture, as deployed on the experimental plot. The particles lay at about 75 cm from the downslope side of the plot.

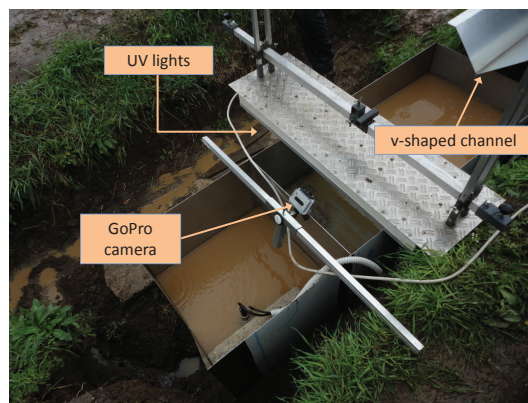


**Figure 12.** Detection unit comprising UV light and video camera for the fluorescent particle identification. The camera captures the surface of the central partition of the collection tank, whereas particles are discharged from the v-shaped aluminum channel.

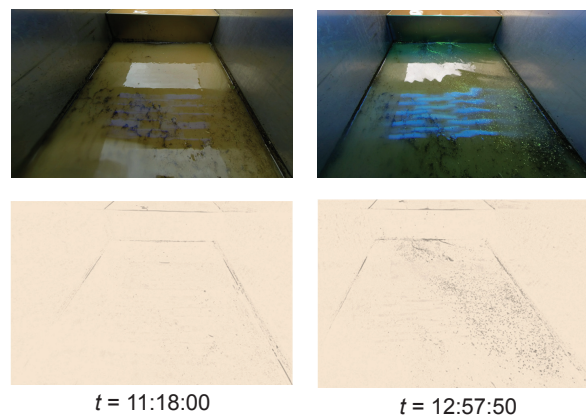


**Figure 13.** Unprocessed (top) and filtered (bottom) snapshots of the second partition of the collection tank during the January 30th event at the particle deployment time (11:18:00, left) and end of the event (12:57:50, right), which depict particle arrival at the detection unit.

### 3. Results

#### 3.1. Hillslope Flow Monitoring

Observation of input rainfall and output water from the experimental plot led to findings in Figure 14. In Figure 14a, cyan bars show input rainfall measurements in mm/5 min and the solid red line displays the output discharge estimated using the rating curve in Section 2.2.1 for the water level sensor. Data are reported up to a couple hours after the cessation of natural rainfall (14:00 on 30 January). The experiment was performed during a fairly heavy rainfall event. Specifically, precipitation was first observed in the afternoon on 29 January. This corresponded to null output discharge from the plot. Significant rainfall was registered at night, leading to a high output discharge peak, and on 30 January from 11:00 to 14:00. Such observations referred to peaks in the output discharge delayed by a few minutes with respect to rainfall peaks. In Figure 14b, the cumulated rainfall curve is depicted as a solid blue line and the cumulated output discharge as a solid red line. We note that less than half of the total rainfall volume was discharged from the experimental plot in the analyzed time interval. The cumulated discharge curve is slightly shifted in time with respect to the cumulated rainfall.

To further investigate the hydrological response of the hillslope to precipitation, in Figure 15, we report soil moisture values recorded by the soil moisture probes. Specifically, measurements ( $W$ ) were normalized by the values obtained at saturation ( $W_{\text{sat}}$ ) and presented in Section 2.2.3. As expected, the moisture conditions of the experimental plot were stable until 2:00, when a rather steep increase was observed at the two shallowest soil moisture probes, that is, DS in the downslope region and US in the uppermost region (refer to Figure 7 for probes naming). For the entire duration of the experiment, higher moisture was recorded from the deeper probe in the downslope region of the hillslope, and, before 2:00, the driest conditions were found in the uppermost region close to the soil surface. These findings are in line with standard hillslope response observed in natural environments and, thus, confirm the suitability of the setup for hydrological monitoring. After 2:00, the shallower probes were the most affected by increasing precipitation and the downslope sensor recorded higher humidity with respect to the deeper one at approximately 13:00.

The soil moisture behavior displayed in Figure 15 suggests that percolation to the deepest soil layers should occur in rather extended periods of time, whereas quicker responses were observed on the plot surface. Specifically, a quantity close to half the total rainfall volume was rapidly discharged from the experimental plot. However, a greater part of precipitation both percolated through the soil and was most probably lost in evapotranspiration phenomena. Inspection of the soil through the glass panels did not result in a clearly detectable infiltration profile.

In Figure 16, we report suspended sediment concentration measurements from the sensing probe and the estimated suspended solid volume in the last partition of the collection tank. The suspended solid volume is estimated by multiplying the suspended sediment concentration in mg/L by the output liquid volume measured in the last partition of the collection tank. Interestingly, a sharp increase in suspended sediment concentration is observed around 12:00, that is, close to the last rainfall peak. Turbidity consistently increased with rainfall until 13:30. After such time, the level in the collection tank decreased and part of the solid material was ejected, thus resulting in decreasing turbidity. As expected, the suspended solid volume closely followed precipitation regime in Figure 14a with peaks registered almost simultaneously with rainfall. These observations suggest that suspended sediment concentration is highly correlated with runoff. In Figure 17, we report pictures of the plot before and after the experiment. Specifically, in the top image, a view of the hill is presented after the experiment, where the dashed box encloses the wetter soil of the downslope contributing area. In the bottom frames, the area where particles were deployed is illustrated at the onset and at the end of the experiment. Due to the geometry of the plot and as illustrated in the right-side image, it was evident that the lower end of the slope was rapidly saturated and contributed to overland flow. This was visually confirmed by the darker soil color and the presence of small-scale rills.

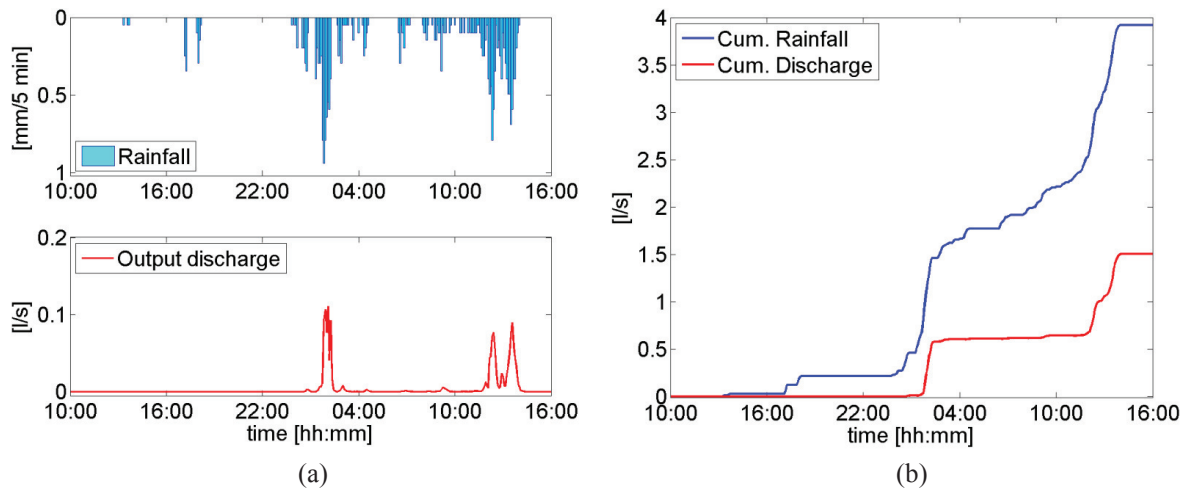


**Figure 14.** (a) input rainfall in mm/5min and output discharge and (b) cumulated rainfall and cumulated output discharge.

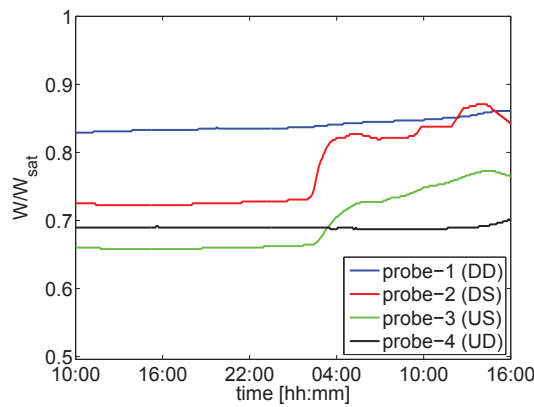


**Figure 15.** Normalized water content as measured by the four soil moisture probes. As in Figure 7, the acronym UD stands for upslope-deep, US for upslope-shallow, DS for downslope-shallow and DD for downslope-deep.

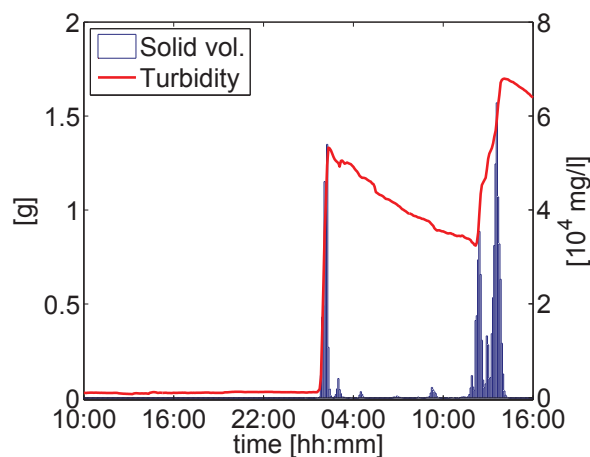


**Figure 16.** Suspended solid volume (vol.) transported during the experiment in g and suspended sediment concentration in mg/L measured at the v-notch gauging tank. Data were collected every 5 min.



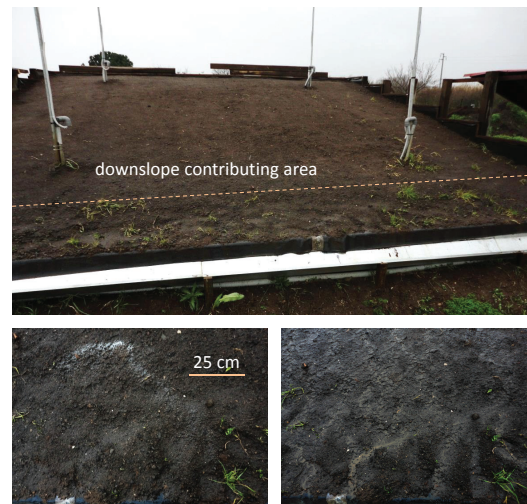


**Figure 17.** (Top) view of the plot after the experiment: the dashed line delimits the saturated downslope contributing area; (bottom) view of the area where particles were deployed before (left) and after (right) the experiment.

### 3.2. Particle Arrival Distribution

In Figure 18, we report the time series of the particle image coverage for the experiment duration. Specifically,  $B_0$  indicates the number of pixels covered by the total amount of beads, and  $B$  denotes the number of pixels covered by particles in each image. We note that pictures were recorded up to about 13:15, that is, until the end of the last major rainfall peak. Each marker in Figure 18 corresponds to a picture. Interestingly, the curve can be regarded as a standard tracer breakthrough curve, where the canonical S-shape is clearly distinguishable. In particular, particle arrivals at the detection unit were noted from the very beginning of the experiment. This is attributed to a number of factors; namely, particles were manually deployed from a height of 1 m from the soil surface; therefore, meager quantities of tracers were placed closer to the v-shaped aluminum channel due to wind effects. Furthermore, rain-splash contributed to the particles' discontinuous displacement in the downslope direction. Starting from 12:24:30, the presence of particles in the tank increased sharply. From 12:57:50, the slope of the curve decreased suggesting that particles' arrival rate was also lowering. We note that markers found at lower values in the curve at approximately 12:30 and close to the end of the experiment are relative to interruption of the test for close-up checks of the camera. Out of the total amount of particles deployed, 97% was recovered. Most of the remaining particles was observed to lay on the sides of the v-shaped channel.

At the beginning of the experiment, no rills were visible with a naked eye on the soil surface. Drainage organization was closely monitored during the particle test, and visual observation of the plot suggested that the sharp increase in the particle breakthrough curve corresponded to the formation of small-scale rills, which acted as preferential flow paths for water and sediments (see also Figure 17). As a small scale rill network was established, particle transport became more consistent.

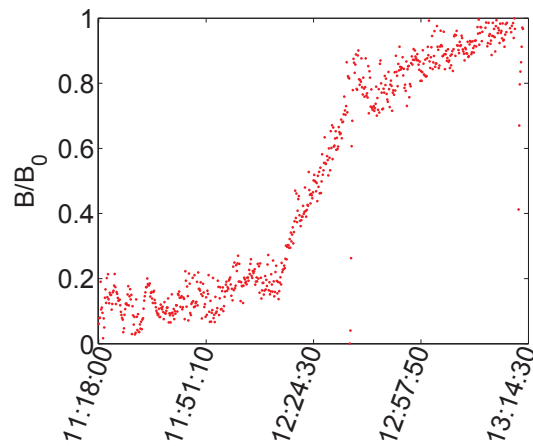


**Figure 18.** Tracer particle arrivals at the monitoring station (times are relative to the storm on 30 January). The symbol  $B_0$  indicates the number of pixels covered by the total amount of deployed beads, and  $B$  denotes the number of pixels covered by particles in each image. The presence of fluorescent particles on the surface of the water tank is derived from their surface coverage in captured images.

### 3.3. Experimental Plot Water Budget

We estimate the water budget at Cape Fear for the observed event (from 29 January at 10:00 to 30 January at 16:00) by applying the hydrological water balance equation ( $P = Q + \Delta W + ET$ , whereby  $P$  indicates rainfall volumes,  $Q$  is runoff,  $\Delta W$  refers to the change in soil water content, and  $ET$  indicates evapotranspiration). Total rainfall was equal to  $1.18 \text{ m}^3$  and runoff was computed to be  $0.45 \text{ m}^3$ . We determined  $\Delta W$  as the difference in the soil water content before and after the illustrated precipitation event. Soil water content was computed from soil moisture probes observations as follows. The difference in soil water content measured by the four probes at the end and beginning of the precipitation event was computed. Soil moisture values from different probes were weighed with the plot volumes sensed by each sensor and then summed. We estimated that a total of  $0.68 \text{ m}^3$  of water infiltrated during the event. Evapotranspiration was indirectly estimated to be equal to  $0.05 \text{ m}^3$  from the hydrological water balance equation. Table 3 reports details on peak values in the observed rainfall, runoff, and turbidity, as well as the total suspended solid volume, and contributions to the plot water budget. Two main peaks were identified in the observed event.

**Table 3.** Peak values and water budget for the illustrated rainfall event.

	Peak Values	Time at Peak	Water Budget	
Rainfall [mm/5min]	0.94	30 January at 1:50	$P$ [ $\text{m}^3$ ]	1.18
Runoff [L/s]	0.11	30 January at 2:05	$\Delta W$ [ $\text{m}^3$ ]	0.68
Turbidity [mg/L]	53,251.90	30 January at 2:20	$Q$ [ $\text{m}^3$ ]	0.45
Rainfall [mm/5min]	0.79	30 January at 12:20	$ET$ [ $\text{m}^3$ ]	0.05
Runoff [L/s]	0.09	30 January at 13:35	Total suspended solid volume [g]	
Turbidity [mg/L]	67,973.55	30 January at 14:05		17.4

## 4. Discussion and Conclusions

In this preliminary study, we assessed the feasibility of studying runoff onset in hybrid experimental settings by dissecting the response of Cape Fear to natural rainfall in case of unvegetated cover. We remark that, at the time the experiment was performed, the soil did not present previous surface preferential pathways. Furthermore, the soil was relatively uniform, the plot presented a uniform slope, the waterproof layer replicated the effect of a totally impermeable bedrock, and the soil depth to the impermeable layer varied proportionally to the upslope distance from the discharge measuring point.

As reported in Section 3, experimental observations pointed out a quick response of the system to input rainfall. Specifically, discharge was slightly delayed with respect to precipitation, and a quantity close to half ( $0.45 \text{ m}^3$ ) the total rainfall volume was rapidly discharged during the precipitation event. Most of rained water ( $0.68 \text{ m}^3$ ) infiltrated in the plot. In fact, upper soil moisture probes (US and DS) showed abrupt increases in proximity of rainfall. As confirmed by post-event observations, water content monitored through DS and US probes decreased after the event. On the other hand, deeper soil moisture probes were poorly affected by the storm. In the aftermath of the event, in fact, probe UD registered increasing soil moisture values, thus suggesting infiltration phenomena to the deeper soil upslope. Probe DD registered slowly decreasing soil moisture values. As expected, the downslope region of the plot was the quickest to be saturated during the rainfall event given its shallow soil depth.

Interestingly, turbidity was more delayed with respect to rainfall and output discharge. In particular, with regards to the second rainfall peak (at 12:20), particle arrivals started to drastically increase since 12:24. and runoff peaked at 13:35, while the peak in turbidity was achieved around 14:00. The sharp increase in particle arrivals corresponded to saturation in the downslope area and to the formation of preferential surface pathways, that led to rill formation.

In accordance with the experimental setup, saturation excess overland flow was the driving mechanism leading to Cape Fear hydrological response [1], thus demonstrating the well-functioning of the plot. In particular, saturation excess runoff was experienced in the wetter soil at the base of the hillslope, see the DD probe in Figures 15 and 17. At the location of the DD probe, soil moisture values close to saturation were observed and saturation was further attested by the darker soil color in the most downslope area of the plot. Figure 15 depicts the normalized water content measured by the soil moisture probes. The probes located in the downslope area of the plot (DS and DD) monitored higher values of soil-water content than the upslope probes. This was consistently found throughout the year. In particular, in the five days preceding the experiment, recorded water contents were within 3% of values relative to 29 January at 10:00. In response to rainfall, water content sharply increased in the downslope shallow soil layer and it slowly increased in the deeper layer. During the storm, the wetter downslope area expanded upslope, as confirmed by captured pictures of the plot, thus resulting in increasing and slightly delayed output discharge. As larger areas were connected during the storm, preferential flow paths were established and overland flow occurred in small scale rills proximal to the wetter downslope area of the plot. This behavior was supported by turbidity observations: the response delayed by less than half an hour with respect to runoff in the second peak in Figure 16 suggests the contribution of the downslope saturated area.

The proposed particle tracer-based approach opens interesting avenues on the quantitative estimation of the contribution and timing of surface fluxes to overall output discharge. As demonstrated through fluorescent particle motion, the plot immediately responded to external rainfall through subsurface flow. After more than an hour since the beginning of the precipitation event, overland flow was systematically established in saturated areas of the plot.

Despite the promise of the experimental findings, Cape Fear presents a few limitations and, therefore, results observed in the plot may differ from more complex natural conditions. Most importantly, the facility is laterally confined and its soil is homogeneous. This hampers investigations on complex subsurface phenomena. Furthermore, its limited extent prevents the establishment of complex flow patterns. Even if the simple experimental conditions simulated in the plot are rarely found in natural settings, they can be instrumental to isolate specific hydrological processes. Indeed, we expect the observatory to provide future insight on runoff generation processes in different hydrological conditions [64–68]. In particular, some of the outstanding questions to be further investigated at the Cape Fear laboratory are:

- How do the soil structure, vegetation, and spatial pathways evolve over time? How do such changes affect connectivity and the overall response of the plot?
- How do surface morphology and flow pattern organization influence surface transport processes?
- How do rills evolve as a function of slope, length, and vegetation in natural rainfall conditions?

Such research questions will be addressed through the integration of multiple sensing systems and by adjusting the plot to the specific experimental conditions. To enhance comprehension of soil behavior during runoff generation, future investigations will be performed by installing full-range tensiometers at different depths and positions in the plot. Furthermore, a hillslope-scale evaporation experiment will be designed for the inverse determination of the soil hydraulic properties. Finally, simulations with HYDRUS 2/3D (PC-Progress, Prague, Czech Republic) will be executed for improved description of lateral flow. Similar to Section 3.2, the use of image-based techniques will be regularly implemented for studying the onset of runoff. Furthermore, this non-invasive methodology will enable the investigation of surface flow dynamics in upland areas. Camera-based observations will be complemented by continuous monitoring of the soil and humidity conditions and input and output fluxes in the hillslope system. Moreover, a removable covering apparatus will be implemented to mitigate the effect of external wind while rainfall simulators are operated.

Ongoing work focuses on the installation of a denser system of sensors to fully dissect the role of soil in runoff formation. An in-depth characterization of soil properties at the plot-scale and the influence of different parameters, such as the use of different soil covers, diverse rill slopes and lengths, and the presence of vegetation, on runoff formation will be soon undertaken.

**Acknowledgments:** This work was supported by the Ministero degli Affari Esteri project 2015 Italy-USA PGR00175 and the UNESCO Chair in Water Resources Management and Culture. The authors would like to greatly acknowledge Roberto Rapiti, Giuliano Cipollari, Paolo Valerio Ciorba, and Massimo Vollaro for developing the hillslope plot and helping with the experiments.

**Author Contributions:** All authors conceived and designed the experiments; F.T., A.P., N.R., M.Palladino and S.G. performed the experiments; F.T., A.P. and M.Palladino analyzed the data; and all authors wrote the paper.

**Conflicts of Interest:** The authors declare no conflict of interest. The founding sponsors had no role in the design of the study; in the collection, analyses, or interpretation of data; in the writing of the manuscript, and in the decision to publish the results.

## References

1. Dunne, T. *Field Studies of Hillslope Flow Processes*; Wiley: London, UK, 1978; Chapter 7, pp. 227–293.
2. Weiler, M.; McDonnell, J.J. Virtual experiments: A new approach for improving process conceptualization in hillslope hydrology. *J. Hydrol.* **2004**, *285*, 3–18.
3. Janzen, D.; McDonnell, J.J. A stochastic approach to modelling and understanding hillslope runoff connectivity dynamics. *Ecol. Model.* **2015**, *298*, 64–74.
4. Hewlett, J.D. *Soil Moisture as a Source of Base Flow From Steep Mountain Watersheds*; Station Paper 132; US Forest Service, Southeastern Forest Experiment Station: Asheville, NC, USA, 1961.
5. Hewlett, J.D.; Hibbert, A.R. Moisture and energy conditions within a sloping soil mass during drainage. *J. Geophys. Res.* **1963**, *68*, 1081–1087.
6. Dunne, T.; Black, R.D. An experimental investigation of runoff production in permeable soils. *Water Resour. Res.* **1970**, *6*, 478–490.
7. Dunne, T.; Black, R.D. Partial area contributions to storm runoff in a small New England watershed. *Water Resour. Res.* **1970**, *6*, 1296–1311.
8. Anderson, M.G.; Burt, T.P. Automatic monitoring of soil moisture conditions in a hillslope spur and hollow. *J. Hydrol.* **1977**, *33*, 27–36.
9. Anderson, M.G.; Burt, T.P. A laboratory model to investigate the soil moisture conditions on a draining slope. *J. Hydrol.* **1977**, *33*, 383–390.
10. Bonell, M. Selected challenges in runoff generation research in forests from the hillslope to headwater drainage basin scale. *J. Am. Water Resour. Assoc.* **1998**, *34*, 765–785.
11. Kendall, C.; McDonnell, J.J.; Gu, W. A look inside “black box” hydrograph separation models: A study at the Hydrohill catchment. *Hydrol. Process.* **2001**, *15*, 1877–1902.
12. McGuire, K.J.; Weiler, M.; McDonnell, J.J. Integrating tracer experiments with modeling to assess runoff processes and water transit times. *Adv. Water Resour.* **2007**, *30*, 824–837.



13. Montgomery, D.R.; Dietrich, W.E.; Torres, R.; Anderson, S.P.; Heffner, J.T.; Loague, K. Hydrologic response of a steep, unchanneled valley to natural and applied rainfall. *Water Resour. Res.* **1997**, *33*, 91–109.
14. Anderson, S.P.; Dietrich, W.E.; Montgomery, D.R.; Torres, R.; Conrad, M.E.; Loague, K. Subsurface flow paths in a steep, unchanneled catchment. *Water Resour. Res.* **1997**, *33*, 2637–2653.
15. Anderson, S.P.; Dietrich, W.E.; Torres, R. Concentration-discharge relationships in runoff from a steep, unchanneled catchment. *Water Resour. Res.* **1997**, *33*, 211–225.
16. Freer, J.; McDonnell, J.J.; Beven, K.J.; Peters, N.E.; Burns, D.A.; Hooper, R.P.; Aulenbach, B.; Kendall, C. The role of bedrock topography on subsurface storm flow. *Water Resour. Res.* **2002**, *38*, 1269.
17. Tromp-van Meerveld, H.J.; McDonnell, J.J. Threshold relations in subsurface stormflow: 1. A 147-storm analysis of the Panola hillslope. *Water Resour. Res.* **2006**, *42*, W02410.
18. Tromp-van Meerveld, H.J.; McDonnell, J.J. Threshold relations in subsurface stormflow: 2. The fill and spill hypothesis. *Water Resour. Res.* **2006**, *42*, W02411.
19. Klaus, J.; Zehe, E.; Elsner, M.; Külls, C.; McDonnell, J.J. Macropore flow of old water revisited: Experimental insights from a tile-drained hillslope. *Hydrol. Earth Syst. Sci.* **2013**, *17*, 103–118.
20. McGlynn, B.L.; McDonnell, J.J.; Brammer, D.D. A review of the evolving perceptual model of hillslope flowpaths at the Maimai catchments, New Zealand. *J. Hydrol.* **2002**, *257*, 1–26.
21. Blöschl, G.; Blaschke, A.P.; Broer, M.; Bucher, C.; Carr, G.; Chen, X.; Eder, A.; Exner-Kittridge, M.; Farnleitner, A.; Flores-Orozco, A.; et al. The Hydrological Open Air Laboratory (HOAL) in Petzenkirchen: A hypotheses driven observatory. *Hydrol. Earth Syst. Sci. Discuss.* **2015**, *12*, 6683–6753.
22. Gerwin, W.; Schaaf, W.; Biemelt, D.; Fischer, A.; Winter, S.; Hüttl, R.F. The artificial catchment “Chicken Creek” (Lusatia, Germany)—A landscape laboratory for interdisciplinary studies of initial ecosystem development. *Ecol. Eng.* **2009**, *35*, 1786–1796.
23. Bachmair, S.; Weiler, M.; Troch, P.A. Intercomparing hillslope hydrological dynamics: Spatio-temporal variability and vegetation cover effects. *Water Resour. Res.* **2012**, *48*, W05537.
24. Zhu, T.X.; Cai, Q.G.; Zeng, B.Q. Runoff generation on a semi-arid agricultural catchment: Field and experimental studies. *J. Hydrol.* **1997**, *196*, 99–118.
25. Brooks, E.S.; Boll, J.; McDaniel, P.A. A hillslope-scale experiment to measure lateral saturated hydraulic conductivity. *Water Resour. Res.* **2004**, *40*, W04208.
26. Scherrer, S.; Naef, F.; Faeh, A.O.; Cordery, I. Formation of runoff at the hillslope scale during intense precipitation. *Hydrol. Earth Syst. Sci.* **2007**, *11*, 907–922.
27. Wainwright, J.; Parsons, A.J.; Abrahams, A.D. Plot-scale studies of vegetation, overland flow and erosion interactions: Case studies from Arizona and New Mexico. *Hydrol. Process.* **2000**, *14*, 2921–2943.
28. Li, M.H.; Chibber, P. Overland flow time of concentration on very flat terrains. *Transp. Res. Rec. J. Transp. Res. Board* **2008**, *2060*, 133–140.
29. Ghahramani, A.; Ishikawa, Y.; Gomi, T.; Shiraki, K.; Miyata, S. Effect of ground cover on splash and sheetwash erosion over a steep forested hillslope: A plot-scale study. *Catena* **2011**, *85*, 34–47.
30. Esteves, M.; Faucher, X.; Galle, S.; Vauclin, M. Overland flow and infiltration modelling for small plots during unsteady rain: Numerical results versus observed values. *J. Hydrol.* **2000**, *228*, 265–282.
31. Kampf, S.K.; Burges, S.J. Parameter estimation for a physics-based distributed hydrologic model using measured outflow fluxes and internal moisture states. *Water Resour. Res.* **2007**, *43*, W12414.
32. Hopp, L.; Harman, C.; Desilets, S.L.E.; Graham, C.B.; McDonnell, J.J.; Troch, P.A. Hillslope hydrology under glass: Confronting fundamental questions of soil-water-biota co-evolution at Biosphere 2. *Hydrol. Earth Syst. Sci.* **2009**, *13*, 2105–2118.
33. Niu, G.Y.; Pasetto, D.; Scudeler, C.; Paniconi, C.; Putti, M.; Troch, P.A.; DeLong, S.B.; Dontsova, K.; Pangle, L.; Breshears, D.D.; et al. Incipient subsurface heterogeneity and its effect on overland flow generation—Insight from a modeling study of the first experiment at the Biosphere 2 Landscape Evolution Observatory. *Hydrol. Earth Syst. Sci.* **2014**, *18*, 1873–1883.
34. Nieber, J.L.; Walter, M.F. Two-dimensional soil moisture flow in a sloping rectangular region: Experimental and numerical studies. *Water Resour. Res.* **1981**, *17*, 1722–1730.
35. Bryan, R.B.; Poesen, J. Laboratory experiments on the influence of slope length on runoff, percolation and rill development. *Earth Surf. Process. Landf.* **1989**, *14*, 211–231.
36. He, J.J.; Sun, L.Y.; Gong, H.L.; Cai, Q.G.; Jia, L.J. The characteristics of rill development and their effects on runoff and sediment yield under different slope gradients. *J. Mt. Sci.* **2016**, *13*, 397–404.

37. Michaelides, K.; Wainwright, J. Internal testing of a numerical model of hillslope-channel coupling using laboratory flume experiments. *Hydrol. Process.* **2008**, *22*, 2274–2291.
38. Fang, H.; Sun, L.; Tang, Z. Effects of rainfall and slope on runoff, soil erosion and rill development: An experimental study using two loess soils. *Hydrol. Process.* **2015**, *29*, 2649–2658.
39. Tauro, F.; Aureli, M.; Porfiri, M.; Grimaldi, S. Characterization of buoyant fluorescent particles for field observations of water flows. *Sensors* **2010**, *10*, 11512–11529.
40. Tauro, F.; Pagano, C.; Porfiri, M.; Grimaldi, S. Tracing of shallow water flows through buoyant fluorescent particles. *Flow Meas. Instrum.* **2011**, *26*, 93–101.
41. Tauro, F.; Mocio, G.; Rapiti, E.; Grimaldi, S.; Porfiri, M. Assessment of fluorescent particles for surface flow analysis. *Sensors* **2012**, *12*, 15827–15840.
42. Tauro, F.; Grimaldi, S.; Petroselli, A.; Rulli, M.C.; Porfiri, M. Fluorescent particle tracers in surface hydrology: A proof of concept in a semi-natural hillslope. *Hydrol. Earth Syst. Sci.* **2012**, *16*, 2973–2983.
43. Riley, S.J.; Hancock, F. A rainfall simulator for hydrologic and erosion experiments on mines, with an example of its applications at Ranger Uranium Mine, Northern Territory, Australia. *Aust. Inst. Min. Metall. Proc.* **1997**, *1*, 3–8.
44. Gee, W.G.; Or, D. *Methods of Soil Analysis*; Chapter Particle-Size Analysis; Soil Science Society of America: Madison, WI, USA, 2002; pp. 255–293.
45. Mebius, L. A rapid method for the determination of organic carbon in soil. *Anal. Chim. Acta* **1960**, *22*, 120–124.
46. Topp, G.C.; Ferré, P.A. *Methods of Soil Analysis: Part 4—Physical Methods*; Chapter Water Content; Soil Science Society of America: Madison, WI, USA, 2002; Volume 5, pp. 417–446.
47. Reynolds, W.D.; Elrick, D.E.; Youngs, E.G.; Amoozegar, A.; Booltink, H.W.G. *Methods of Soil Analysis, Part 4—Physical Methods*; Chapter Saturated and Field-Saturated Water Flow Parameters; Soil Science Society of America: Madison, WI, USA, 2002; pp. 797–878.
48. Ciollaro, G.; Romano, N. Spatial variability of the hydraulic properties of a volcanic soil. *Geoderma* **1995**, *65*, 263–282.
49. Romano, N.; Hopmans, J.W.; Dane, J.H. *Methods of Soil Analysis, Part 4—Physical Methods*; Chapter Water Retention and Storage—Suction Table; Soil Science Society of America: Madison, WI, USA, 2002; pp. 692–698.
50. Dane, J.H.; Hopmans, J.W. *Methods of Soil Analysis: Part 4—Physical Methods*; Chapter Pressure Plate Extractor; Soil Science Society of America: Madison, WI, USA, 2002; pp. 688–690.
51. Romano, N.; Santini, A. Determining soil hydraulic functions from evaporation experiments by a parameter estimation approach: Experimental verifications and numerical studies. *Water Resour. Res.* **1999**, *35*, 3343–3359.
52. Romano, N.; Angulo-Jaramillo, R.; Javaux, M.; vanderPloeg, M.J. Interweaving monitoring activities and model development towards enhancing knowledge of soil-plant-atmosphere continuum. *Vadose Zone J.* **2012**, *11*, 1–6.
53. Romano, N.; Santini, A. *Methods of Soil Analysis, Part 4—Physical Methods*; Chapter Water Retention and Storage: Field; Soil Science Society of America: Madison, WI, USA, 2002; pp. 721–738.
54. Bos, M. *Discharge Measurement Structures*; Technical Report 20; International Institute for Land Reclamation and Improvement/ILRI: Wageningen, The Netherlands, 1989.
55. Grimaldi, S.; Petroselli, A.; Baldini, L.; Gorgucci, E. Description and preliminary results of a 100 square meter rain gauge. *J. Hydrol.* **2015**, ISSN 0022-1694, doi:10.1016/j.jhydrol.2015.09.076.
56. Pérez-Latorre, F.J.; deCastro, L.; Delgado, A. A comparison of two variable intensity rainfall simulators for runoff studies. *Soil Tillage Res.* **2010**, *107*, 11–16.
57. Chouksey, A.; Lambey, V.; Nikam, B.R.; Aggarwal, S.P.; Dutta, S. Hydrological modelling using a rainfall simulator over an experimental hillslope plot. *Hydrology* **2017**, *4*, 17.
58. Christiansen, J.E. The uniformity of application of water by sprinkler system. *Agric. Eng.* **1941**, *22*, 89–92.
59. Atlas, D.; Srivastava, R.C.; Sekhon, R.S. Doppler radar characteristics of precipitation at vertical incidence. *Rev. Geophys.* **1973**, *11*, 1–35.
60. Lhermitte, R.M. Probing of atmospheric motion by airborne pulse-Doppler radar techniques. *J. Appl. Meteorol.* **1971**, *10*, 234–246.
61. Gunn, R.; Kinzer, G.D. The terminal velocity of fall for water droplets in stagnant air. *J. Meteorol.* **1949**, *6*, 243–248.
62. Löffler-Mang, M. An optical disdrometer for measuring size and velocity of hydrometeors. *J. Atmos. Ocean. Technol.* **2000**, *17*, 130–139.

63. Forsyth, D.A.; Ponce, J. *Computer Vision: A Modern Approach*; Prentice-Hall: New York, NY, USA, 2002.
64. Rosso, R.; Rulli, M.C. An integrated simulation method for flash-flood risk assessment: 2. Effects of changes in land-use under a historical perspective. *Hydrol. Earth Syst. Sci.* **2002**, *6*, 285–294.
65. Rulli, M.C.; Bozzi, S.; Spada, M.; Bocchiola, D.; Rosso, R. Rainfall simulations on a fire disturbed mediterranean area. *J. Hydrol.* **2006**, *327*, 323–338.
66. Fiori, A.; Russo, D. Numerical analyses of subsurface flow in a steep hillslope under rainfall: The role of the spatial heterogeneity of the formation hydraulic properties. *Water Resour. Res.* **2007**, *43*, W07445.
67. Fiori, A.; Romanelli, M.; Cavalli, D.J.; Russo, D. Numerical experiments of streamflow generation in steep catchments. *J. Hydrol.* **2007**, *339*, 183–192.
68. Fiori, A.; Russo, D. Travel time distribution in a hillslope: Insight from numerical simulations. *Water Resour. Res.* **2008**, *44*, W12426.



© 2017 by the authors. Licensee MDPI, Basel, Switzerland. This article is an open access article distributed under the terms and conditions of the Creative Commons Attribution (CC BY) license (<http://creativecommons.org/licenses/by/4.0/>).